Les Cahiers du GERAD ISSN: 0711–2440

Microstructured surface design for ice nucleation control assisted by a hybrid Classical Nucleation Theory-blackbox approach

S. Keshavarzi, O. Gagné, O. Zacharie, S. Séguin, G. Momen, H. Tremblay

G–2026–05

January 2026

La publication de ces rapports de recherche est rendue possible grâce au soutien de HEC Montréal, Polytechnique Montréal, Université McGill, Université du Québec à Montréal, ainsi que du Fonds de recherche du Québec – Nature et technologies.

Dépôt légal – Bibliothèque et Archives nationales du Québec, 2026
– Bibliothèque et Archives Canada, 2026

The publication of these research reports is made possible thanks to the support of HEC Montréal, Polytechnique Montréal, McGill University, Université du Québec à Montréal, as well as the Fonds de recherche du Québec – Nature et technologies.

Legal deposit – Bibliothèque et Archives nationales du Québec, 2026
– Library and Archives Canada, 2026

GERAD HEC Montréal
3000, chemin de la Côte-Sainte-Catherine
Montréal (Québec) Canada H3T 2A7

Tél. : 514 340-6053
Téléc. : 514 340-5665
info@gerad.ca
www.gerad.ca

Microstructured surface design for ice nucleation control assisted by a hybrid Classical Nucleation Theory-blackbox approach

Samaneh Keshavarzi [a]

Olivier Gagné [b, c]

Olivier Zacharie [a, b]

Sara Séguin [b, c]

Gelareh Momen [d]

Hugo Tremblay[c]

[a] *Department of Applied Sciences, Université du Québec à Chicoutimi, Saguenay (Qc), Canada, G7H 2B1*

[b] *GERAD, Montréal (Qc), Canada, H3T 1J4*

[c] *Department of Computer Science and Mathematics, Université du Québec à Chicoutimi, Saguenay (Qc), Canada, G7H 2B1*

[d] *École de Technologie Supérieure, Montréal (Qc), Canada, H3C 1K3*

skeshavarz@etu.uqac.ca
ogagne1@etu.uqac.ca
sara.seguin@uqac.ca
gelareh.momen@etsmtl.ca

January 2026
Les Cahiers du GERAD
G–2026–05

Abstract : Designing icephobic surfaces to delay ice formation is crucial for applications like aviation safety and cryopreservation. While Classical Nucleation Theory (CNT) provides a thermodynamic foundation, real-world stochastic effects and complex wetting states make designing these surfaces difficult. The performance of icephobic surfaces is influenced by surface structure. However, finding the best designs for specific environmental conditions is still a challenge. In this work, we introduce a hybrid approach that combines experiments, CNT, and blackbox optimization to predict and optimize ice nucleation time on micropatterned surfaces. Cylindrical SU-8 micropillar arrays with different heights and spacings were created, and the apparent contact angles and freezing delay times were measured at -10 °C and -20 °C. An analytical model was developed to describe the wetting states between the Wenzel and Cassie Baxter regimes, optimizing its parameters using the Mesh Adaptive Direct Search (MADS) algorithm. This approach allows us to estimate contact angles and ice nucleation times for any surface geometry within the studied design space. The predicted contact angles matched experimental results with a mean absolute percentage error (MAPE) of 2.09% ($R^2 = 0.92$) and the approximate nucleation times showed a MAPE of 27.3% ($R^2 = 0.75$). Our method also identified the best micropillar geometries that maximize freezing delay and was validated with an independent dataset, showing strong predictive ability. This work emphasizes the benefit of combining physics-based models with data-driven optimization for rapid design of icephobic surfaces.

Keywords: Water contact angle; ice nucleation time; surface design; Classical Nucleation Theory; blackbox optimization

Acknowledgements: This work was supported by the Natural Sciences and Engineering Research Council of Canada (NSERC) with an NSERC Discovery Grant — RGPIN–2018–06331.

1 Introduction

The onset of the liquid-to-solid phase transition in supercooled water is ice nucleation that is a critical phenomenon in many natural and engineered systems [1, 2]. The control of ice nucleation on surfaces is a critical challenge in areas like aviation safety, renewable energy, cryopreservation and outdoor infrastructure [3, 4]. Ice formation can reduce efficiency and functionality and may also pose significant safety and economic risks [5]. Although Classical Nucleation Theory (CNT) has well represented the basic thermodynamic principles of ice nucleation [6–9], real-world systems often differ from ideal assumptions. This is due to impurities, complex surface interactions, environmental fluctuations, and stochastic effects [3, 10–12].

Micro- and nano-engineered surfaces have recently been used as a passive method to control ice formation. Microstructured surfaces, especially those with periodic designs like micropillars, can change how droplets interact with surfaces by altering wetting behavior, contact line dynamics, and heat transfer [13–18]. Depending on the surface geometry and chemistry, droplets may rest on surface features in a Cassie-Baxter state [19], completely wet the surface in a Wenzel state [20], or fall in the intermediate state [21–23]. Each of these states affects the contact area between solid and liquid, heat transfer, and the energy barrier for nucleation.

While microstructured surfaces can significantly affect droplet wetting and interfacial energy, they do not remove the randomness of ice formation. Ice nucleation is inherently stochastic which means even under seemingly controlled and identical conditions, nucleation events may occur at different times. Eberle et al. [10] demonstrated the random nature of ice nucleation using Poisson statistics, where nucleation events follow a nonhomogeneous Poisson process during cooling and a homogeneous Poisson process at constant temperature. In multiple contexts like pharmaceutical freezing, identical vials can also show a wide range of nucleation times during cold-chain storage and freeze-drying [24]. Another challenge is the complexity of the design space. Surface shapes can have many adjustable factors, including pillar diameter, height, spacing, aspect ratio, and surface chemistry. The properties related to droplets, as well as environmental factors like cooling rate, humidity, and temperature, all play a key role in determining nucleation outcomes. Exploring this multi-faceted space through experimentation alone is very time-consuming and resource-heavy. Additionally, accurately characterizing wetting states on these surfaces especially during dynamic freezing adds to the complexity.

To address these complex and random design challenges, data-driven methods have recently been used to speed up materials and surface design. This includes neural networks, random forests, and other supervised learning models [25–29]. However, they usually require large datasets, may be hard to interpret, and might not easily incorporate theoretical models. In contrast, blackbox optimization (*BBO*) provides a strong alternative. Algorithms like Mesh Adaptive Direct Search (MADS), implemented in NOMAD software [30], have been used in various fields such as energy systems, materials design, hydrology, aerospace, and biomedical engineering [31]. For materials design, for example, blackbox methods have enabled efficient exploration of complex composition spaces, prediction of phase stability, and identification of materials with optimized properties. This makes it especially useful for situations where evaluation is costly or hard to analyze [32]. The advantage of these types of methods is that optimization can be conducted even when there is no analytical representation of the objective function and/or the constraints. In many industrial applications, the objective value can only be computed using a computer code, since the models are complex, unknown and have no explicit mathematical formulation. Blackbox optimization requires only input-output values of the blackbox to optimize the objective function and the constraints, if there are any. One of the greatest advantages of MADS is that it is a provably convergent algorithm, compared to methods issued from the field of machine learning. This algoritm also handles continous, integer and categorical variables, making it suitable for complex applications. MADS is better for optimization when the goal is to find optimal decisions.

In this study, we present a novel hybrid approach that combined experiments, CNT-based calculations, and blackbox optimization (CNT-BBO approach) to approximate ice nucleation time and guide surface design. We created SU-8 micropillar arrays with different geometries and measured both contact angles and nucleation times under controlled subzero conditions. We calculated theoretical nucleation times using CNT while applying an interpolation method to account for partial wetting. Blackbox optimization was then used to merge experimental and theoretical data into an optimization model that estimates contact angles and nucleation times for any surface geometry and suggests the optimum surface design to increase ice nucleation time (Figure 1). The performance of this methodology was tested on new surface designs that had not been evaluated before. The close match between the approximated and experimentally measured contact angles and nucleation times confirms the reliability and usefulness of the approach. This validation shows that the methodology can effectively estimate surface behavior for geometries not included in the original dataset.

Overall, we propose an adaptive framework for microstructured surface design to approximate contact angles and ice nucleation times. By combining experimental data, CNT-based calculations, and blackbox optimization, this approach provides an efficient way to design ice-repelling surfaces.

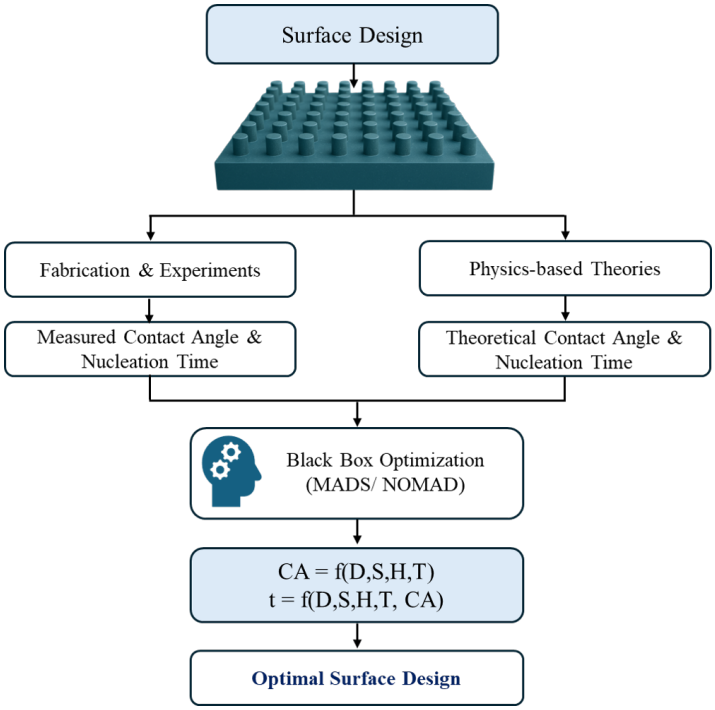

Figure 1: Overall structure of the paper. The key parameters used throughout the study are defined as follows: water contact angle (CA), ice nucleation time (t), pillar diameter (D), pillar height (H), pillar spacing (S), and temperature (T).

2 Methodology

2.1 Surface fabrication & characterization

Micropatterned surfaces were created on silicon wafers using standard photolithography techniques, as we described in our previous work [33]. Arrays of cylindrical SU-8 micropillars were produced with a diameter of 10 μm (D) and heights (H) of 10 or 20 μm. The pillar spacings (S) ranged from 5 to 100 μm, resulting in 14 different surface configurations. Each 15 $\times$ 15 mm sample was chemically modified with trichloro(1H,1H,2H,2H-perfluorooctyl) silane (TPFS) to improve hydrophobicity. We characterized surface morphologies using scanning electron microscopy (SEM) and 3D optical profilometry (Figure 2)

and measured contact angle (CA) using a goniometer at 22 °C, −10 °C, −20 °C; and relative humidity $30 \pm 5\%$.

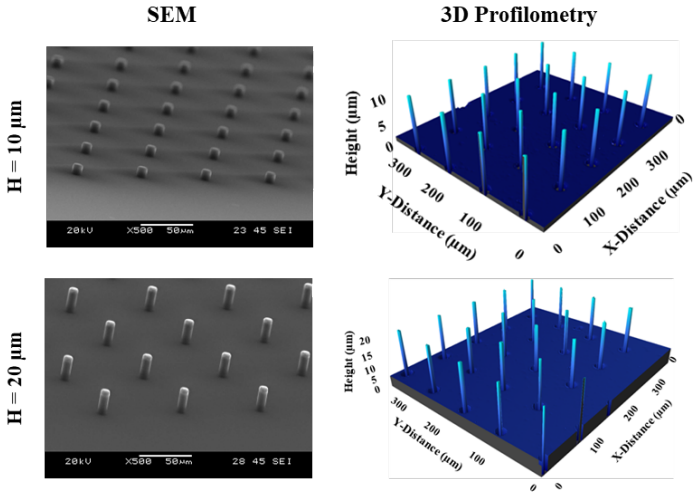

Figure 2: SEM images and 3D surface profile of silicon wafer surface with S = 70 μm.

For ice nucleation experiments (Figure 3), 10 μL deionized water droplets were deposited on the micropillar surfaces inside a temperature-controlled chamber. A high-speed camera recorded the freezing process, and the delay time for ice nucleation was determined from the moment of droplet deposition to visible ice formation. Readers can refer to our original publication [33] for full experimental details. This study builds upon and expands that work to provide an approximating tool for ice nucleation time.

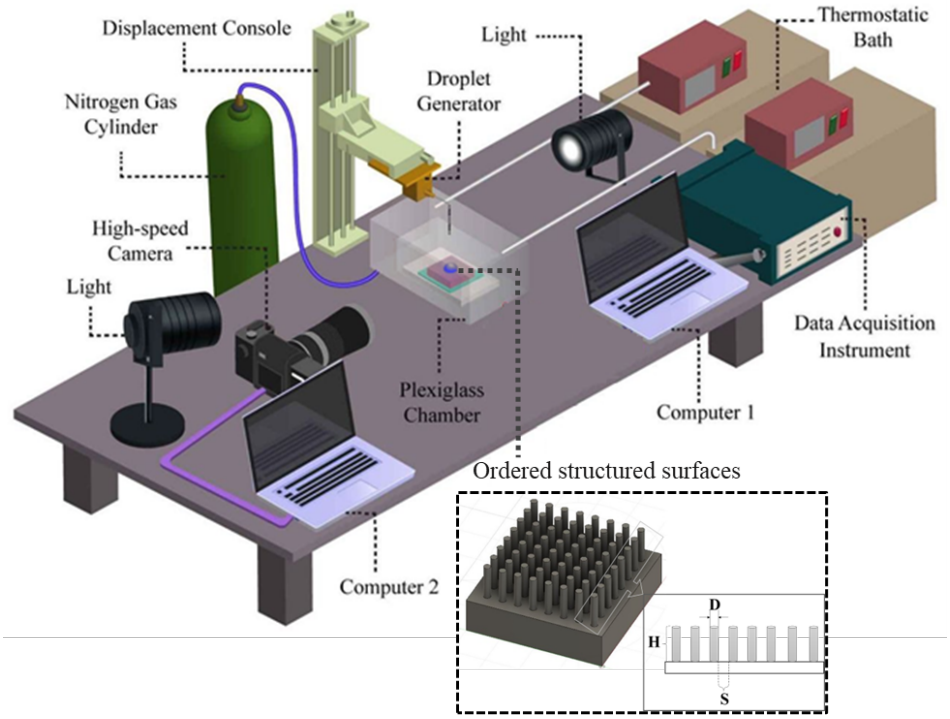

Figure 3: Schematic of the experimental setup [33].

2.2 Wetting models and theoretical framework

The apparent contact angle (θ) of a droplet is governed by the balance of interfacial tensions between the solid, liquid, and vapor phases. For a perfectly smooth surface, Young's equation applies (Figure 4) [34, 35]:

$$\cos(\theta_Y) = \frac{\gamma_{SV} - \gamma_{SL}}{\gamma_{LV}} \tag{1}$$

where γ_{SL}, γ_{LV} and γ_{SV} represent the interface tensions of the solid/liquid, liquid/vapor and solid/vapor, respectively.

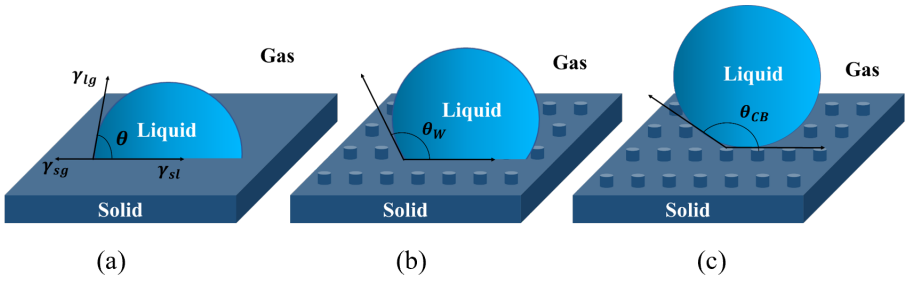

Figure 4: Typical wetting mechanisms (a) Young contact mode (b) Wenzel mode (c) Cassie-Baxter mode.

On rough surfaces, Wenzel and Cassie–Baxter models are defined as following [36–38]:

$$\cos(\theta_W) = r\cos(\theta_Y) \tag{2}$$

$$\cos(\theta_{CB}) = \Phi(1 + \cos(\theta_Y)) - 1 \tag{3}$$

where r is the roughness ratio, Φ is the solid fraction of the surface, θ_W , θ_{CB}, and θ_Y are the Wenzel, Cassie-Baxter and the Young contact angle, respectively.

The calculations of r and Φ are based on the cylindrical surface geometry used in this study [39]:

$$r = \frac{(D+S)^2 + \pi DH}{(D+S)^2} \tag{4}$$

$$\Phi = \frac{\pi D^2}{4(D+S)^2} \tag{5}$$

According to the theory of intermediate wetting [21, 22], the contact angle is described as follows:

$$\cos\theta_{PW} = (\Phi + (r_w - \Phi)f)\cos\theta_Y + (1-\Phi)(1-f)\cos 180^\circ \tag{6}$$

For a droplet in partial wetting state, the effective solid–liquid contact area A (actual contact area considering microstructure penetration) can be approximated by [23]:

$$A = A'\big(\Phi + f(r_W - \Phi)\big) \tag{7}$$

where A' is the projected base area of the droplet on a flat surface. Given droplet volume V and contact angle θ, A' is calculated as [40]:

$$A' = \frac{\left(9\pi V^2\right)^{1/3}\sin^2\theta}{\left((2+\cos\theta)(\cos\theta-1)^2\right)^{2/3}} \tag{8}$$

2.3 Ice nucleation model based on CNT

Heterogeneous nucleation rates are described by CNT as [10, 12]:

$$J(T) = K(T)A \exp\left(-\frac{\Delta G^*_{\text{Hetero}}(T)}{K_B T}\right) \tag{9}$$

In this equation, $K(T)$ is a kinetic factor showing the diffusive flux of water molecules across the ice interface, A is the contact area between the droplet and the substrate, $\Delta G^*_{\text{Hetero}}$ represents the free energy barrier for heterogeneous nucleation, K_B is the Boltzmann constant (1.38×10^{-2} J K^{-1}), and T is the absolute temperature.

The kinetic factor $K(T)$ is expressed as:

$$K(T) = \frac{k_B T}{h} \exp\left(\frac{-k_B T^2 E}{(T - T_R)^2} \Big/ (k_B T)\right) n \tag{10}$$

where $h = 6.62 \times 10^{-34}$ J s^{-1} is Planck's constant, $n \approx 10^{19}$ m^{-2} is the number density of water molecules at the ice interface, $T_R = 118$ K and $E = 892$ K are empirical parameters derived from experiments on supercooled water, valid between 150 K and 273 K [10].

The nucleation barrier $\Delta G^*_{\text{Hetero}}$ for a spherical ice embryo is calculated as:

$$\Delta G^*_{\text{Hetero}} = \frac{16\pi\gamma_{IW}^3}{3(\Delta G_V)^2}\,\phi(\theta) \tag{11}$$

Here, γ_{IW} is the interfacial energy between ice and water, ΔG_V is the volumetric free energy change, and $\phi(\theta)$ is a geometric correction factor that depends on the ice–water contact angle θ_{IW}:

$$\phi(\theta) = \frac{(1 - \cos\theta_{IW})^2(2 + \cos\theta_{IW})}{4} \tag{12}$$

Since θ_{IW} cannot be directly measured, it is inferred by fitting CNT-based predictions of nucleation rates to experimentally measured delay times at different temperatures.

The temperature dependence of the ice-water interfacial tension is given by [41]:

$$\gamma_{IW} = 28 + 0.25(T - 273.15) \tag{13}$$

And the volumetric free energy change for the phase transition is calculated as:

$$\Delta G_V = \frac{T_m - T}{T_m}\,\Delta H_V \tag{14}$$

where $T_m = 273.15$ K is the melting point of ice under atmospheric pressure, and $\Delta H_V = 278$ MJ m^{-3} is the enthalpy of fusion.

Then, the average nucleation time, t, is:

$$t = \frac{1}{J(T)} \tag{15}$$

2.4 Analytical model for contact angle in intermediate wetting states

Since wetting states are not limited to purely Wenzel or Cassie–Baxter regimes, a new equation is introduced to provide an analytical model for intermediate wetting states by interpolating between

these two contact angles. A new transition function is introduced that is very similar to a weighted-sum function; however, the weights are variable:

$$\cos(\theta_p) = f \times c_1 \times \cos(\theta_W) + (1 - f) \times c_2 \times \cos(\theta_{CB}) \tag{16}$$

where θ_p is the calculated intermediate contact angle, f is the transition function, c_1 and c_2 are constants.

The transition function in Equation (16) is given by:

$$f = \frac{1}{1 + e^{-c_3(\frac{S}{H^{0.6}} - c_4)}} \tag{17}$$

where c_3 and c_4 are constants, S is the spacing between the pillars and H is the height of the pillars.

This transition function is based on a simoid function, which is commonly used to represent the transition phenamena. To consider the combined effects of S and H, the term $c_3(\frac{S}{H^{0.6}} - c_4)$ was added to the exponential part of the sigmoid function. The constants c_1 through c_4 in Equation (16) and Equation (17) are determined using blackbox optimization described in the following Sections.

2.5 Parameter optimization via Blackbox

Blackbox optimization is used when the analytical representation of the objective function and/or the constraints are not available. Therefore, the problem is treated as a blackbox and derivatives are not used to conduct optimization. Rather, inputs are given to the blackbox optimization solver, and outputs are observed to refine the solution. Blackbox optimization is often used for hyperparameter tuning, as it is the case for this project. NOMAD [42] is a blackbox optimization software that is the implementation of the MADS algorithm. This algorithm does not used derivatives or gradients, but rather explores the state space using a mesh, that is shrunk of expanded, depending on the solutions at each iteration.

NOMAD proposes inputs for the blackbox, then the user provides the framework to compute the value of the blackbox for theses values of input, and the solution is returned to NOMAD, that returns new values of input to be evaluated. The mesh is then refined or coarsened, and a new iteration is conducted. Usually, a budget of evaluations is given to NOMAD as a stopping criterion.

2.5.1 Calculation of c_1, c_2, c_3, c_4

Figure 5 illustrates the process when NOMAD is used to optimize values for the parameters c_1 to c_4. The blackbox uses the equations defined in Section 2.2 and Section 2.3, and Equations (16)–(18) to calculate the theoretical contact angle θ_p using the theoretical equations given input values c_1 through c_4. The output of the blackbox is given by diff_sum(c_1, c_2, c_3, c_4). The following equation is used to calculate diff_sum:

$$diff\_sum = \sum_{i \in \Omega} |\theta_e^i - \theta_p^i| \tag{18}$$

where Ω is the set of experimental points and θ_e^i are the experimental contact angles.

The sum of the differences between the theoretical contact angle and the experimental contact angle is minimized by the blackbox solver and the best values for c_1, c_2, c_3 and c_4 are obtained.

2.5.2 Calculation of θ_{IW}

Since θ_{IW} cannot be meausred experimentally at the ice–water–substrate interface, the value of this angle is calculated for the intermediate wetting states using the theoretical equations. This value is required to calculate the theoretical nucleation times.

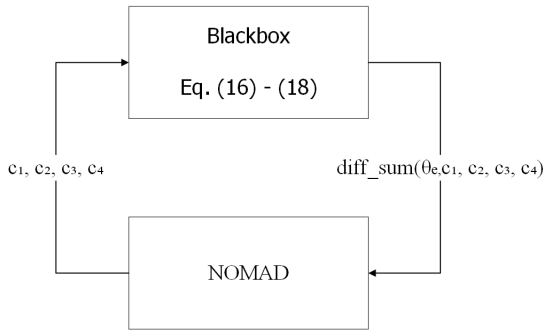

Figure 5: Blackbox optimization procedure used to determine parameters c_1, c_2, c_3, and c_4.

Figure 6 shows the process to calculate θ_{IW} using blackbox optimization. NOMAD proposes a value for θ_{IW}, then the nucleation time is calculated using Equations (2)–(17).

We need to define the equation diff_err, which calculates the error between the theoretical nucelation time calculated with the theoretical Equations (2)–(17) and the experimental nucleation time:

$$diff\_err = \sum_{i \in \Omega} |t_e^i - t_{\theta_{IW}}| \tag{19}$$

where Ω is the set of experimental points, t_e^i are the experimental nucleation times, and $t_{\theta_{IW}}$ are the calculated nucleation times.

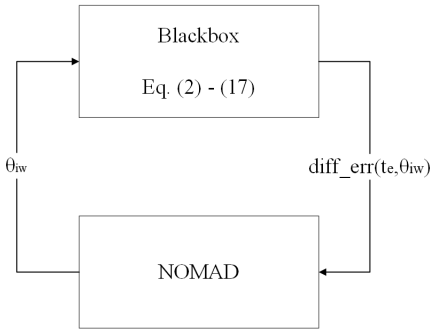

Figure 6: Blackbox optimization procedure for calculating θ_{IW}.

2.5.3 Calculation of the optimal surface design

Given the experimental data, blackbox optimization is also used to calculate the optimal surface design, more precisely to find the best values of S, D and H to maximize the nucleation time for a temperature T of either -10 °C or -20 °C.

Figure 7 shows the process. The blackbox takes as input values of D, H, S and the output is the difference between the nucelation times, calculated using theoretical Equations (2)–(17) and the experimental nucleation times. Note that the temperature T is fixed to -10 °C or -20 °C, and must be used accordingly in the equations.

Calc_time is defined as:

$$calc\_time = \sum_{i \in \Omega} |\lambda_e^i - \lambda_p^i| \tag{20}$$

where Ω is the set of experimental points, λ_e^i are the experimental nucleation times, λ_p^i are the calculated nucleation times given the parameters D, H, S, T.

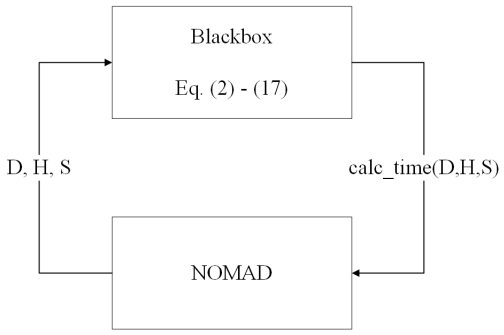

Figure 7: Blackbox optimization procedure for identifying the optimal surface design.

One the budget of evaluations is reached, the best values for D, S and H are found using the blackbox optimization solver NOMAD.

3 Results and discussion

This Section details the results obtained. First, the experimental dataset that was used is detailed. Second, the approximated values for the contact angle, the nucleation time and the optimal surface design are presented. Third, a new dataset is introduced in order to validate the proposed methodology and results are also reported.

3.1 Experimental dataset

The experimental data set used in this study was obtained from measurements performed on 14 micropillar silicon wafer surfaces with fixed pillar diameter D = 10 μm, pillar height H = 10 and 20 μm, and pillar spacing S = 5, 10, 20, 30, 40, 70, and 100μm. The experiments were performed at temperatures T = -10 °C and -20 °C using 10 μL water droplets (V). For each configuration, the apparent contact angle (CA) and ice nucleation time (t) were measured with multiple repetitions. The intrinsic contact angle (θ_Y) was measured on smooth, chemically identical SU-8 substrates. It was found to be 95.9° at -10 °C and 93.3° at -20 °C. These values used as inputs for the wetting and CNT-based nucleation times.

3.2 Approximation of the intermediate contact angle

In our previous work [33], all microstructured silicon wafer surfaces exhibited partial wetting states at both -10 °C and -20 °C. This indicated that neither the pure Cassie–Baxter nor Wenzel models fully explained the actual droplet–surface interaction in our surfaces. In this study, we developed a model to approximate the contact angle in these intermediate states. The theoretical expressions of Cassie–Baxter and Wenzel states were used as bounding conditions and a continuous transition function was introduced to show a smooth transition between them. The model parameters were optimized using the experimental contact angles at -10 °C and -20 °C. The approximate and experimental CA were compared in Figures 8. In these figures, the Cassie-Baxter contact angles, given spacing and height, are shown by the pink surface, the Wenzel contact angles by the green surface, and the propsed transition function by the blue surface. The experimental contact angles are shown as yellow points. It is shown that the experimental data points closely follow the fitted theoretical model (blue surface), confirming that the parameters c_1 through c_4, optimized using the blackbox optimization model, accurately represent the underlying intermediate wetting state. The approximation model also successfully reproduces the observed increase in contact angle with decreasing pillar spacing and increasing height. This is expected because reduced solid–liquid contact area improves hydrophobicity.

In theory, the contact angle for partial wetting is described by the intermediate wetting model as shown in Equation (6) [20, 21]. Here, the effective solid-liquid contact ratio f determines the shift between the Wenzel and Cassie-Baxter states that depends on geometric features and the fractal characteristics of the surface, expressed as $f = 1 - \Phi^{D-2}$ [21]. To find D experimentally, it is needed to conduct a detailed fractal analysis of high-resolution surface images using the box-counting method [43]. This process is time-consuming, sensitive to imaging conditions, and often produces uncertain results. Consequently, theoretical approximations based on this formulation may diverge from experimental observations when surface variation or partial liquid penetration takes place.

The current model addresses these limitations by using a data-driven transition function instead of explicitly calculating f and D. This function uses the combined effects of geometric parameters like S, H, and D. The sigmoid-type transition interpolates between the Cassie-Baxter and Wenzel limits that allows for continuous approximation of the contact angle. The model obtained a mean absolute percentage error of 2.09% (MAPE), a median error of 1.07% and an R^2 of 0.92. The optimized parameters are $c_1 = 0.58300675119152$, $c_2 = 5.65445621119218$, $c_3 = 2.58164406154465$, and $c_4 = 0.90242543026997$. This good agreement between approximated and experimental contact angles shows the capability of the proposed method in the intermediate wetting behavior on micropatterned surfaces. The ability to estimate contact angles accurately for new surface can provide a basis for measuring ice nucleation time. Since the contact angle affects the solid-liquid contact area and the heterogeneous nucleation barrier, this approximation model can be used for assessing how different designs may influence nucleation behavior.

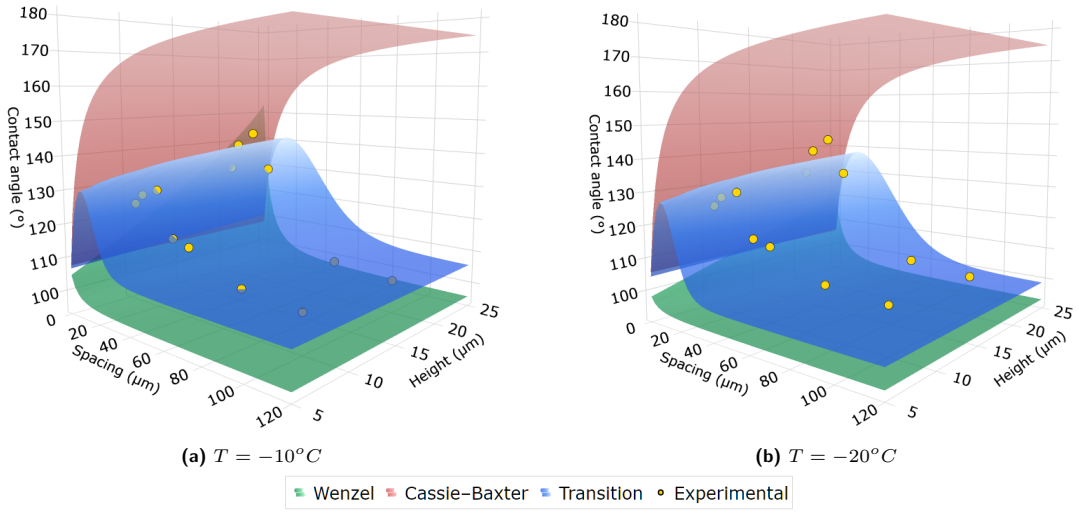

Figure 8: Water contact angle (CA) of the silicon wafer surfaces at (a) T = −10 °C and (b) T = −20 °C.

3.3 Approximation of the ice nucleation time

Figures 9 compares the measured freezing delay times with the approximations made by the hybrid CNT-BBO approach. The boxplots show the observed distribution of nucleation times, while the curves represent the three CNT-based predictions: (i) the Wenzel model (green solid line), (ii) the Cassie-Baxter model (orange dotted line), and (iii) the partial-wetting transition model proposed in this work (blue dotted line). The blue dotted line shows the nucleation times calculated using optimized θ_{IW_p} by blackbox optimization. For each value of S, the boxplots show the experimental variability. The whiskers indicate the minimum and maximum values, the horizontal line inside the box represents the median, and the lower and upper parts of the box correspond to the 25% and 75% of the data, respectively.

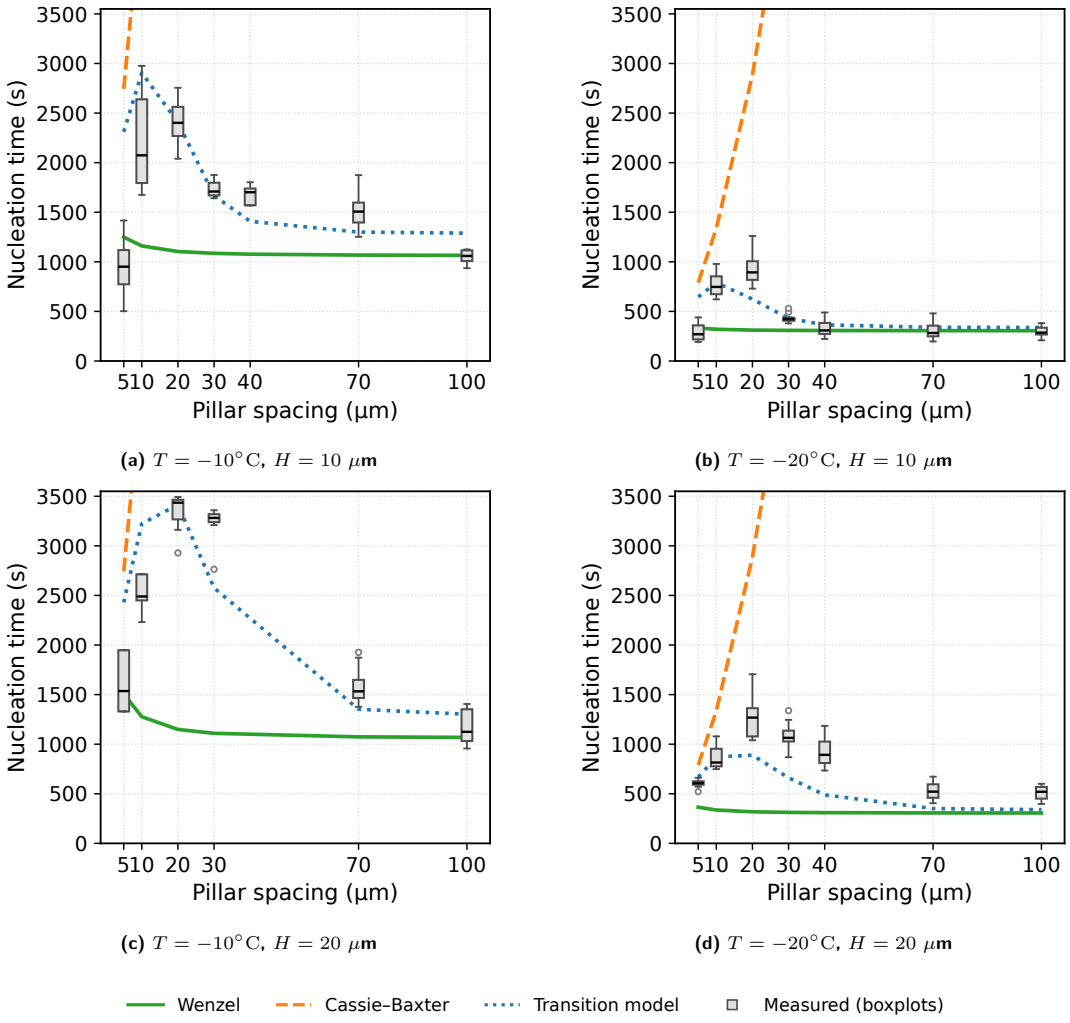

(a) $T = -10°\text{C}$, $H = 10\ \mu\text{m}$ **(b)** $T = -20°\text{C}$, $H = 10\ \mu\text{m}$

(c) $T = -10°\text{C}$, $H = 20\ \mu\text{m}$ **(d)** $T = -20°\text{C}$, $H = 20\ \mu\text{m}$

Figure 9: Ice nucleation times on the micropillar silicon wafer surfaces with $H = 10\ \mu$m at (a) T = $-10\ °$C and (b) T = $-20\ °$C, and $H = 20\ \mu$m at (c) T = $-10\ °$C and (d) T = $-20\ °$C.

As illustrated, the transition-based model fits well with the experimental nucleation times across all pillar spacings, temperatures, and pillar heights. While the transition model does not perfectly follow the median of the data, it captures the overall variability and trends. The predicted trends match the observed increase in freezing delay as spacing increases from 5 to 20 μm, followed by a decrease at larger spacings. This aligns with the wetting behavior discussed earlier. In contrast, the two classical CNT models do not capture the measured trends. The Wenzel model consistently underestimates nucleation times because it assumes full liquid penetration and maximum solid-liquid contact. The Cassie-Baxter model, on the other hand, reliably overestimates nucleation times, especially at larger spacings, due to its ideal assumption of minimal contact area. These differences are clear under all experimental conditions shown in Figures 9, where both limiting models diverge significantly from the observed distributions.

A quantitative error analysis further highlights the strength of the transition-based model. Using the predicted intermediate contact angle, the framework achieved a mean absolute percentage error (MAPE) of 27.3%, a median absolute percentage error of 16.2%, and an overall coefficient of determination of $R^2 = 0.75$ across all geometries and temperatures.The predicted θ_{IW_p} were 49.6918425404838° for $-10\ °$C and 83.38854995304851° for $-20\ °$C. Notably, using experimentally measured contact

angle values instead of predicted ones led to slightly worse performance (MAPE = 28.7%, median = 19.8%, $R^2 = 0.70$). This indicates that the contact-angle approximation model improves the accuracy of the nucleation-time estimation.

Overall, the results show that the hybrid CNT- BBO framework provides reliable, strong, and physically consistent approximations of ice nucleation time across a wide range of micropillar geometries. By combining heterogeneous nucleation theory with data-driven optimization, the approach effectively captures both the geometric dependence of wetting states and the thermodynamics involved in ice formation. This validated predictive ability supports the reliable design of microstructured surfaces aimed at maximizing freezing delay.

3.4 Optimal surface design

While using the blackbox optimisation on our model at -10 °C and -20 °C, we obtain that the optimal surface design for the domain of our data at -10 °C is a diameter D of 10 μm, a height H of 20 μm and a spacing S of 16 μm, which gives a nucleation time of 4,479 s. At a temperature of -20 °C, the optimal surface design is very similar with only the spacing changing from 16 μm to 15 μm which gives a nucleation time of 808 s.

Based on these results, synthetic data was generated using the theoretical equations and the methodology used in the paper, more precisely calculation of the transition function and then the nucleation time. The following domain of the data was used to generate new data: $D = 10$, $H \in [10, 20]$ and $S \in [5, 100]$, which actually relects the range of the experimental data.

Results are reported with cumulative probability functions for fixed temperatures of T=-10 °C and T=-20 °C as shown in Figures 10 and 11, respectively. Bars show the probability of nucleation times within each bin with the left y-axis, and the red curve shows the cumulative probability distribution (CDF), with the right y-axis. For example, in Figure 11a, there is a 0.005 probability that the nucleation time is rougly between to 675 s to 677 s and a probability of 1 that the nucleation time is below 800 s.

Only S between 13 μm to 18 μm are shown since these values are close to the optimal surface design of 16 μm. These figures illustrate the cumulative distribution function of the nucleation time, highlighting the probability that it remains below a given threshold. For instance, Figure 10d shows that there is a 0.45 probability that the nucleation time is less than 4,000 s.

3.5 Model validation

To further assess the methodology proposed in this work, a dataset from a previously published study was used for validation [44]. The dataset includes ice nucleation time and contact angle of silicone rubber surfaces patterned with cylindrical pillar arrays, obtained at $T = -20$°C. The investigated samples were made of two series of micropillar geometries. In the first series, the pillars had D = 80 $\pm$ 5 μm with H = 85 $\pm$ 5 μm and S = 45, 70, 95, 120, and 145 μm. In the second series, the pillar diameter was increased to D = 110 $\pm$ 5 μm, while the pillar height remained constant at H = 85 $\pm$ 5 μm; the corresponding spacing were S = 15, 40, 65, 90, 115, 140, 165, and 190 μm.

Because the experimental data showed no variation in D and this new validation dataset had a constant H, Equation (17) was modified as follow:

$$f = \frac{1}{1 + e^{-c_3\left(\frac{S}{D^{0.6}} - c_4\right)}}, \tag{21}$$

This modification ensures that the transition function captures the characteristics of the new dataset. The methodology remains consistent with Section 2.5: first, the parameters c_1 throught c_4 in Equation (16) and Equation (21) were optimized using the blackbox optimization solver, and

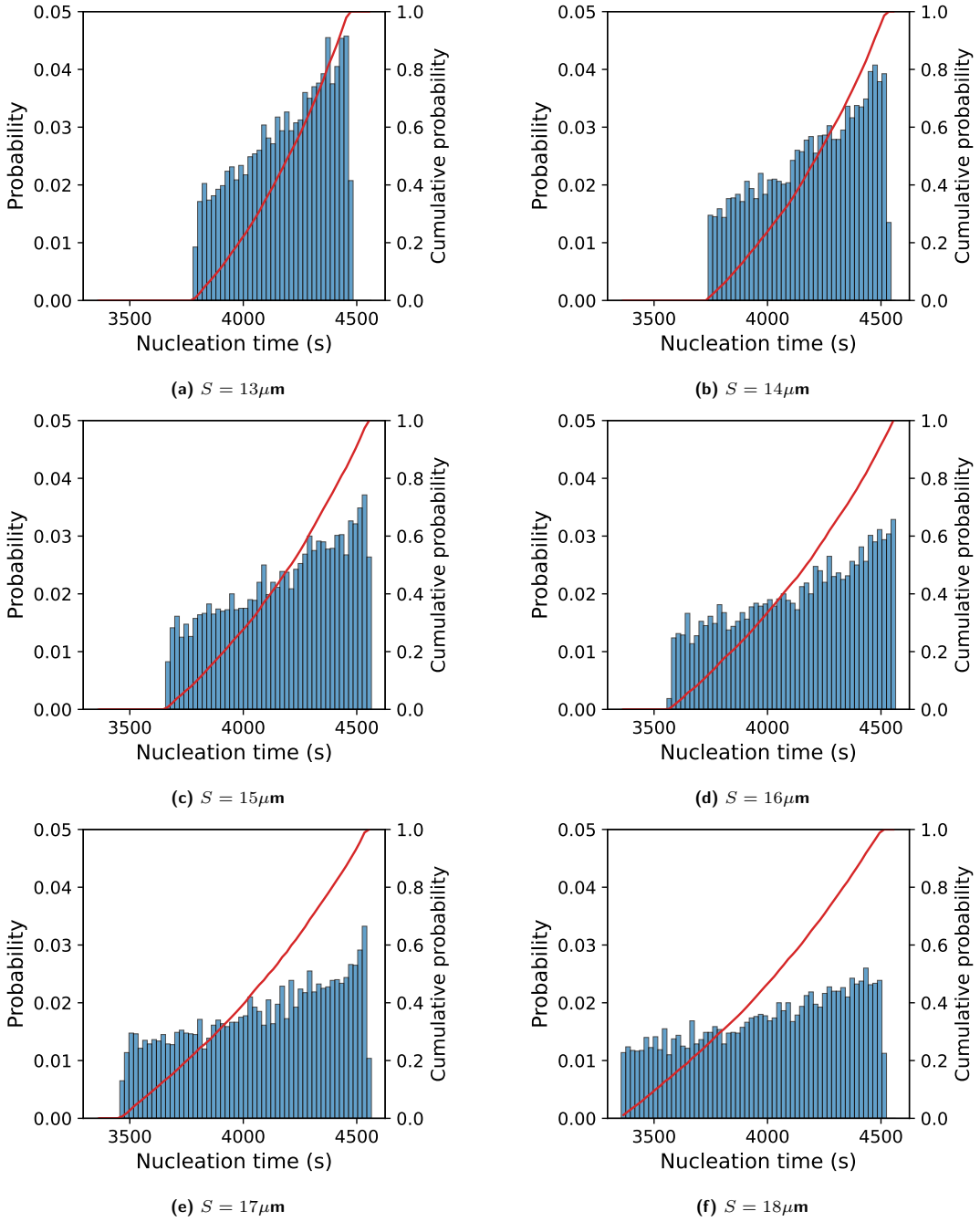

(a) $S = 13\mu$**m** **(b)** $S = 14\mu$**m**

(c) $S = 15\mu$**m** **(d)** $S = 16\mu$**m**

(e) $S = 17\mu$**m** **(f)** $S = 18\mu$**m**

Figure 10: Cumulative distribution functions of ice nucleation times at $T = -10°\mathrm{C}$**.**

then θ_{IW_p} was optimized to approximate the nucleation times. The resulting optimal values were found to be $c_1 = 0.850612298291391$, $c_2 = 14.04238361348403$, $c_3 = 31.26153083647016$, and $c_4 = 0.87504551822843$.

Figure 12 presents the results: the red surface shows the Cassie-Baxter contact angles, for different values of spacing and diameter and a fixed temperature $T = -20°\mathrm{C}$, the green surface shows the Wenzel contact angles, and the blue surface corresponds to the transition function for intermediate wetting states. The yellow dots indicate the validation dataset point. The close proximity of the transition surface to these data points confirms an accurate estimation of the contact angles, and

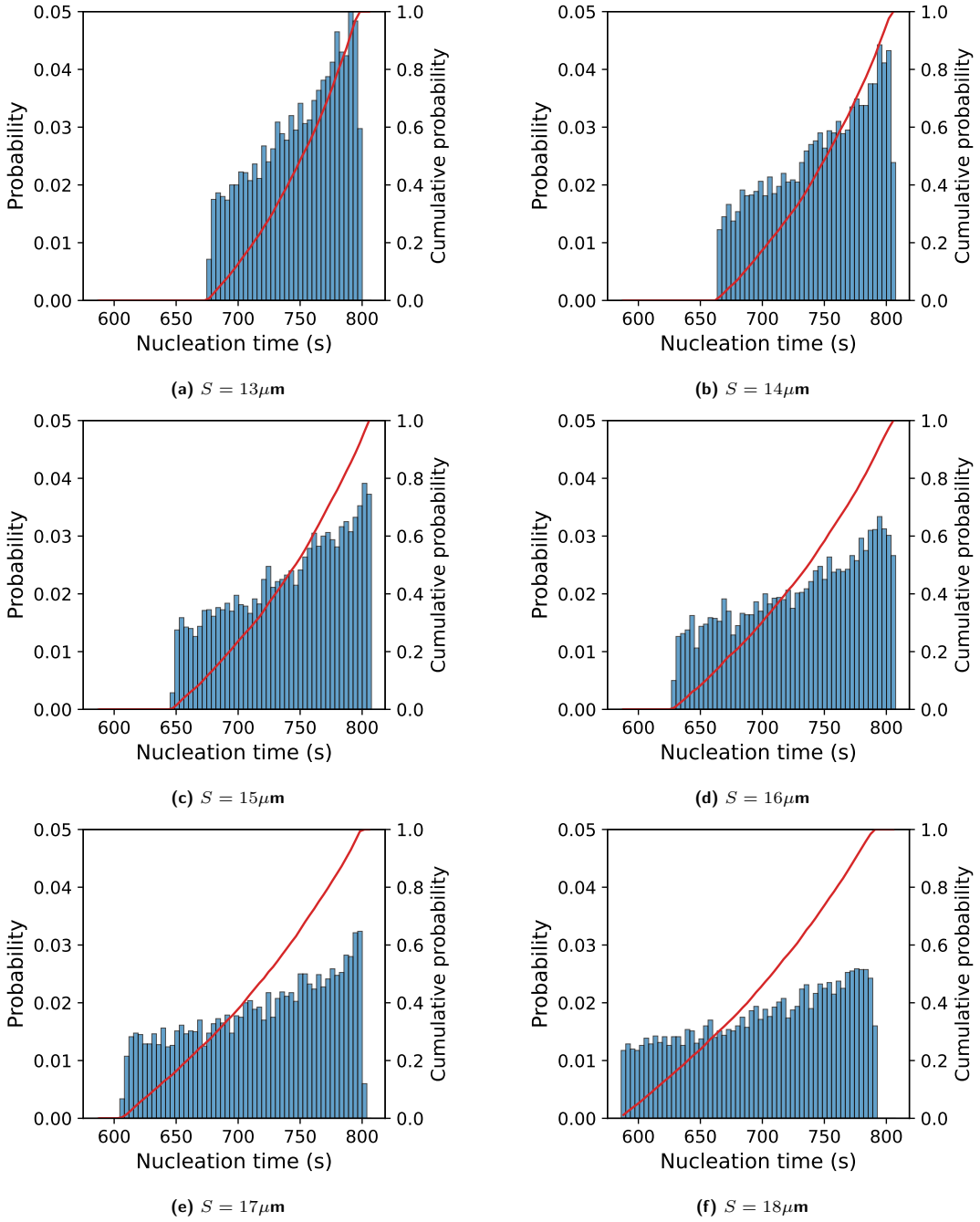

(a) $S = 13\mu$**m** **(b)** $S = 14\mu$**m**

(c) $S = 15\mu$**m** **(d)** $S = 16\mu$**m**

(e) $S = 17\mu$**m** **(f)** $S = 18\mu$**m**

Figure 11: Cumulative distribution functions of ice nucleation times at $T = -20°\mathrm{C}$**.**

validates the methodology. The MAPE for the approximation of the contact angle in intermediate wetting state is 1.55%, with a median of 1.17% and an R^2 is 0.88, further demonstrating the reliability of the methodology.

Using the optimized transition function, θ_{IW_p} was estimated via blackbox optimization to calculate the nucleation time on the new validation dataset. Figure 13 presents these results, where the boxplots indicate the experimental validation data and the green line represnt the approximate nucleation time predicted using the transition function. Although the dataset exhibits significant variability, the

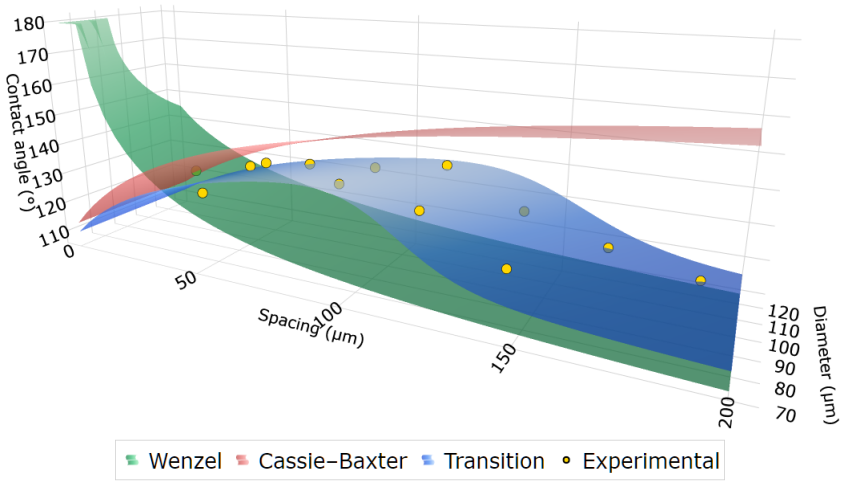

Figure 12: Validation of water contact angle on silicone rubber surfaces at $T = -20°\mathrm{C}$ with pillar diameters of (a) $D = 80$ μm and (b) $D = 110$ μm.

transition function captures the underlying distribution well and follows the overall trend of the data, closely aligning with the allure of the boxplots, leading to a validation of the proposed methodology.

The Statistics for the nucelation delay time showed a MAPE of 29.97, a median of 28.35 and an R^2 of 0.55. While the correlation is moderate, it is reasonable considering the variability in the validation dataset. For comparison, using the experimental contact angle from the validation dataset in the theoretical equations produced a MAPE of 20.57, a median of 25.84, and an R^2 of 0.61. The similarity between these results confirms the validity of the proposed methodology.

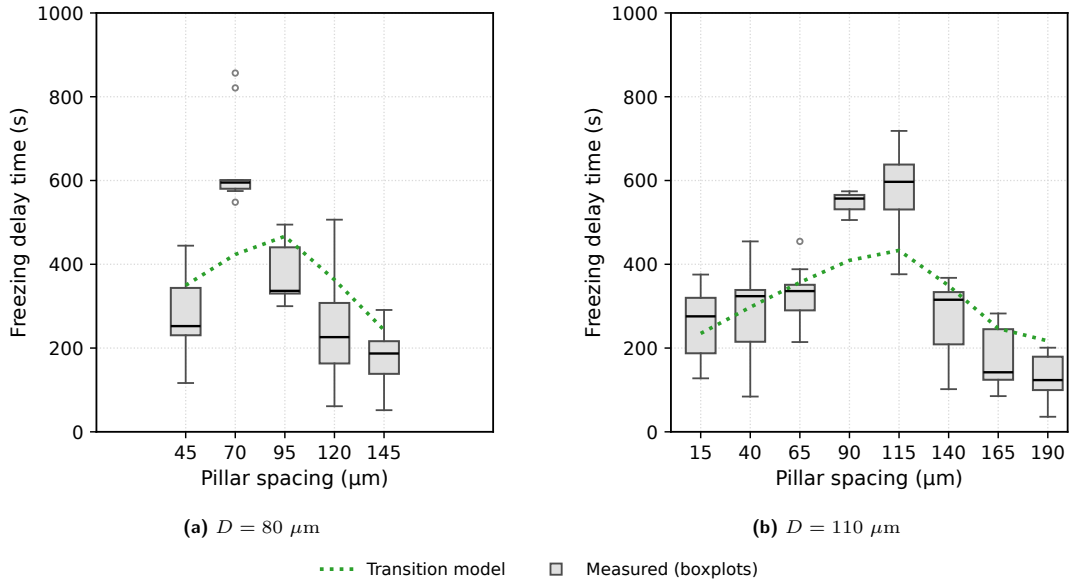

Figure 13: Validation of ice nucleation time approximations for silicone rubber surfaces at $T = -20°\mathrm{C}$ with pillar diameters of (a) $D = 80$ μm and (b) $D = 110$ μm.

4 Conclusion

This study introduced a hybrid framework that combines experimental measurements, Classical Nucleation Theory, and blackbox optimization to estimate contact angles, ice nucleation times, and help design microstructured icephobic surfaces. By directly addressing intermediate wetting states found on micropatterned surfaces, which Wenzel and Cassie-Baxter models do not accurately represent, this approach tackles a major limitation in current ice nucleation models. We developed a sigmoid-based analytical transition function to interpolate between different wetting regimes. This function was calibrated using blackbox optimization. Our model effectively matched experimentally measured contact angles with low errors and strong correlations. It demonstrated the ability to capture the geometric influence on partial wetting without needing complex fractal analysis or direct measurements of penetration parameters. When paired with CNT, the framework offered consistent predictions of ice nucleation times. It successfully matched experimental trends concerning pillar spacing, height, and temperature.

In addition to predictions, the introduced approach identified optimal surface designs that maximize nucleation delays. It showed that intermediate pillar spacings lead to the longest freezing times under the tested conditions. Validation with an independent dataset with different materials and geometries confirmed the reliability and applicability of the method, despite the natural variability of ice nucleation.

Overall, this work shows that merging physics-based models with data-driven blackbox optimization is a strong and effective approach for exploring complex design challenges in icephobic surface engineering. The framework serves as a practical tool for predicting ice nucleation behavior on new surface geometries and can easily adapt to other materials, environmental conditions that involve stochastic nucleation and intricate surface interactions.

References

[1] Daniel A Knopf and Peter A Alpert. Atmospheric ice nucleation. Nature Reviews Physics, 5(4):203–217, 2023.

[2] Yanlong Zhan, Zhenqian Pang, and Gang Tan. Advances in icephobic coatings: Concepts, mechanisms, classifications and prospects. Cold Regions Science and Technology, page 104596, 2025.

[3] G John Morris and Elizabeth Acton. Controlled ice nucleation in cryopreservation–a review. Cryobiology, 66(2):85–92, 2013.

[4] Lingfeng Zhao, Yizhou Shen, Jie Tao, Weilan Liu, Ting Wang, and Senyun Liu. Review on icephobicity of materials surface enhanced by interface action force. Advanced Materials Interfaces, 12(6):2400665, 2025.

[5] Peyman Irajizad, Sina Nazifi, and Hadi Ghasemi. Icephobic surfaces: Definition and figures of merit. Advances in colloid and interface science, 269:203–218, 2019.

[6] Julius Frenkel. A general theory of heterophase fluctuations and pretransition phenomena. The Journal of Chemical Physics, 7(7):538–547, 1939.

[7] R Becker and W Doring. The kinetic treatment of nuclear formation in superheated vapors. Ann Phys, 24:719–752, 1935.

[8] Max Volmer. Nucleus formation in supersaturated systems. Z. Phys. Chem., 119:277–301, 1926.

[9] JY Yan and GN Patey. Molecular dynamics simulations of ice nucleation by electric fields. The Journal of Physical Chemistry A, 116(26):7057–7064, 2012.

[10] Patric Eberle, Manish K Tiwari, Tanmoy Maitra, and Dimos Poulikakos. Rational nanostructuring of surfaces for extraordinary icephobicity. Nanoscale, 6(9):4874–4881, 2014.

[11] Thomas M Schutzius, Stefan Jung, Tanmoy Maitra, Patric Eberle, Carlo Antonini, Christos Stamatopoulos, and Dimos Poulikakos. Physics of icing and rational design of surfaces with extraordinary icephobicity. Langmuir, 31(17):4807–4821, 2015.

[12] D Turnbull and J Co Fisher. Rate of nucleation in condensed systems. Journal of chemical Physics, 17(1):71–73, 1949.

[13] Wenqing Hou, Yizhou Shen, Jie Tao, Yangjiangshan Xu, Jiawei Jiang, Haifeng Chen, and Zhenfeng Jia. Anti-icing performance of the superhydrophobic surface with micro-cubic array structures fabricated by plasma etching. Colloids and Surfaces A: Physicochemical and Engineering Aspects, 586:124180, 2020.

[14] Chunfang Guo, Meiju Zhang, and Jun Hu. Icing delay of sessile water droplets on superhydrophobic titanium alloy surfaces. Colloids and Surfaces A: Physicochemical and Engineering Aspects, 621:126587, 2021.

[15] Wei Xing, Zu Li, Haiou Yang, Xinlin Li, Xinyun Wang, and Ning Li. Anti-icing aluminum alloy surface with multi-level micro-nano textures constructed by picosecond laser. Materials & design, 183:108156, 2019.

[16] Xinlin Li, Guoyong Wang, Ana Sofia Moita, Chengchun Zhang, Shunhao Wang, and Yan Liu. Fabrication of bio-inspired non-fluorinated superhydrophobic surfaces with anti-icing property and its wettability transformation analysis. Applied Surface Science, 505:144386, 2020.

[17] Jing Li, Yijie Zhou, Weibing Wang, Chengyu Xu, and Luquan Ren. Superhydrophobic copper surface textured by laser for delayed icing phenomenon. Langmuir, 36(5):1075–1082, 2020.

[18] Thanh-Binh Nguyen, Seungchul Park, and Hyuneui Lim. Effects of morphology parameters on anti-icing performance in superhydrophobic surfaces. Applied Surface Science, 435:585–591, 2018.

[19] ABD Cassie and SJToTFS Baxter. Wettability of porous surfaces. Transactions of the Faraday society, 40:546–551, 1944.

[20] Robert N Wenzel. Resistance of solid surfaces to wetting by water. Industrial & engineering chemistry, 28(8):988–994, 1936.

[21] Gyoko Nagayama and Dejian Zhang. Intermediate wetting state at nano/microstructured surfaces. Soft Matter, 16(14):3514–3521, 2020.

[22] Yankun Yu, Dejian Zhang, and Gyoko Nagayama. Estimation of surface free energy at microstructured surface to investigate intermediate wetting state for partial wetting model. Soft Matter, 19(6):1249–1257, 2023.

[23] Dejian Zhang, Satoko Takase, and Gyoko Nagayama. Measurement of effective wetting area at hydrophobic solid–liquid interface. Journal of Colloid and Interface Science, 591:474–482, 2021.

[24] Leif-Thore Deck, Andraž Košir, and Marco Mazzotti. Modeling the freezing process of aqueous solutions considering thermal gradients and stochastic ice nucleation. Chemical Engineering Journal, 483:148660, 2024.

[25] Mohammad Autif Shahdhaar, Arpan Srivastava, and Atul Srivastava. Machine learning-aided investigation of immiscible droplet impact on liquid pools across varying depths and droplet viscosities. Experiments in Fluids, 65(3):31, 2024.

[26] Biplab Kumar Roy, Deepak Kumar Mandal, and Amitava Mandal. Investigation of droplet impact dynamics on textured cylindrical hydrophobic surfaces. Colloids and Surfaces A: Physicochemical and Engineering Aspects, 680:132674, 2024.

[27] Pablo Montero de Hijes, Salvatore Romano, Alexander Gorfer, and Christoph Dellago. The kinetics of the ice–water interface from ab initio machine learning simulations. The Journal of Chemical Physics, 158(20), 2023.

[28] Rahul Ramachandran. Using neural networks to predict icephobic performance. arXiv preprint arXiv:2008.00966, 2020.

[29] Ying Zhang and Chen Ling. A strategy to apply machine learning to small datasets in materials science. Npj Computational Materials, 4(1):25, 2018.

[30] Charles Audet, Sébastien Le Digabel, Viviane Rochon Montplaisir, and Christophe Tribes. Algorithm 1027: Nomad version 4: Nonlinear optimization with the mads algorithm. ACM Transactions on Mathematical Software (TOMS), 48(3):1–22, 2022.

[31] Stéphane Alarie, Charles Audet, Aïmen E Gheribi, Michael Kokkolaras, and Sébastien Le Digabel. Two decades of blackbox optimization applications. EURO Journal on Computational Optimization, 9:100011, 2021.

[32] Aïmen E Gheribi, AD Pelton, E Bélisle, Sébastien Le Digabel, and J-P Harvey. On the prediction of low-cost high entropy alloys using new thermodynamic multi-objective criteria. Acta Materialia, 161:73–82, 2018.

[33] Samaneh Keshavarzi, Gelareh Momen, Patric Eberle, Amir Azimi Yancheshme, Nicolas J Alvarez, and Reza Jafari. Exploiting intermediate wetting on superhydrophobic surfaces for efficient icing prevention. Journal of colloid and interface science, 670:550–562, 2024.

[34] Thomas Young. Iii. an essay on the cohesion of fluids. Philosophical transactions of the royal society of London, (95):65–87, 1805.

[35] Randy Doyle Hazlett. Fractal applications: wettability and contact angle. Journal of Colloid and Interface Science, 137(2):527–533, 1990.

[36] Bernd Mockenhaupt, Hans-Jurgen Ensikat, Manuel Spaeth, and Wilhelm Barthlott. Superhydrophobicity of biological and technical surfaces under moisture condensation: stability in relation to surface structure. Langmuir, 24(23):13591–13597, 2008.

[37] Aurélie Lafuma and David Quéré. Superhydrophobic states. Nature materials, 2(7):457–460, 2003.

[38] Ka Lum, David Chandler, and John D Weeks. Hydrophobicity at small and large length scales, 1999.

[39] Khosrow Maghsoudi, Elham Vazirinasab, Gelareh Momen, and Reza Jafari. Advances in the fabrication of superhydrophobic polymeric surfaces by polymer molding processes. Industrial & Engineering Chemistry Research, 59(20):9343–9363, 2020.

[40] Stefan Jung, Marko Dorrestijn, Dominik Raps, Arindam Das, Constantine M Megaridis, and Dimos Poulikakos. Are superhydrophobic surfaces best for icephobicity? Langmuir, 27(6):3059–3066, 2011.

[41] R Scott Smith and Bruce D Kay. The existence of supercooled liquid water at 150? k. Nature, 398(6730):788–791, 1999.

[42] C. Audet, S. Le Digabel, V. Rochon Montplaisir, and C. Tribes. Algorithm 1027: NOMAD version 4: Nonlinear optimization with the MADS algorithm. ACM Transactions on Mathematical Software, 48(3):35:1–35:22, 2022.

[43] Kayhan Foroutan-pour, Pierre Dutilleul, and Donald L Smith. Advances in the implementation of the box-counting method of fractal dimension estimation. Applied mathematics and computation, 105(2–3):195–210, 1999.

[44] Samaneh Keshavarzi, Bassem Bouazara, Gelareh Momen, and Reza Jafari. Hydrophobicity and icephobicity of micropillared silicone rubber surfaces fabricated by compression molding. Results in Surfaces and Interfaces, 12:100132, 2023.